PCCP

ROYAL SOCIETY OF CHEMISTRY

PAPER

View Article Online
View Journal | View Issue

Cite this: *Phys. Chem. Chem. Phys.*, 2024, **26**, 20511

An investigation of the structural and electronic origins of enhanced chemical looping air separation performance of B-site substituted $SrFe_{1-x}Co_xO_{3-\delta}$ perovskites†

Qianwenhao Fan, [ab] Haiyan Li,[c] Syed Saqline, [abd] Felix Donat, [e] Mingwu Tan,[f] Longgang Tao,[f] Christoph R. Müller, [e] Zhichuan J. Xu [g] and Wen Liu *[abd]

Received 25th May 2024,
Accepted 15th July 2024

DOI: 10.1039/d4cp02152e

rsc.li/pccp

Chemical looping air separation (CLAS) is a promising process intensification technology for extracting oxygen from air for oxygen enrichment in process streams. Co-doped strontium ferrites ($SrFe_{1-x}Co_xO_{3-\delta}$) have been found to have outstanding activities for CLAS processes. In this study, we explore the underlying factors driving the enhancement in oxygen uptake and release performance of perovskite structured $SrFe_{1-x}Co_xO_{3-\delta}$ oxygen carriers for CLAS. Phase-pure perovskites, with B site substituted by up to 75 mol% Co, were prepared by a sol–gel method and systematically investigated through a wide range of well controlled experimental and computational approaches. While all $SrFe_{1-x}Co_xO_{3-\delta}$ oxygen carriers showed excellent cyclic stability and structural reversibility over CLAS cycles, increased B site occupancy by Co resulted in monotonic decrease in onset temperature for oxygen release and increase in oxygen carrying capacity. These experimental trends can be fundamentally explained by an increase in the structural tolerance factor, an elevation in transition metal d-band, as well as an increased degree of hybridization between the metal d-band and the O p band. Therefore, these *ab initio* structural and electronic descriptors are useful design rationales for the hypothesis-driven synthesis of high-performing oxygen carriers for CLAS.

1 Introduction

Air separation is a common process in many industrial applications. It plays a crucial role in the production of essential processing gases such as oxygen, nitrogen, and argon, which are extensively used in steel production, oil and gas refining, chemical manufacturing, healthcare, and semiconductors manufacturing.[1,2] Traditional methods of air separation, including cryogenic distillation and pressure swing adsorption, have been the standard practices in industry for many years.[3] Cryogenic distillation, which separates air components based on their different boiling points, is particularly prevalent owing to its ability to produce high-purity gases at large scales. However, cryogenic air separation is a highly energy-intensive process and requires significant capital investment.[4] Pressure swing adsorption (PSA), on the other hand, separates gases based on their molecular characteristics such as size and polarity. While less energy-intensive than cryogenic distillation, PSA is generally less efficient and produces gases of lower purity.[2] In addition, membrane-based methods have also been developed to achieve air separation.[5] By using semi-permeable membranes to separate gases based on their interaction with the membrane materials, air separation may be energy-efficient and simple to operate. However, reliable and high-performance membranes are rare while the energy penalties for operating membrane units are still high.[6] Given the limitations of existing air separation technologies, there is an interest to develop novel air separation technologies that are energy efficient, cost-effective, and environmentally friendly.

Chemical looping air separation (CLAS) has emerged as a promising alternative to existing air separation approaches.[7]

[a] *School of Chemistry, Chemical Engineering and Biotechnology, Nanyang Technological University, 62 Nanyang Drive, Singapore 637459, Singapore. E-mail: wenliu@ntu.edu.sg*
[b] *Cambridge Centre for Advanced Research and Education in Singapore, 1 Create Way, Singapore 138602, Singapore*
[c] *College of Chemical and Biological Engineering, Zhejiang University, Hangzhou, 310027, China*
[d] *Nanyang Environmental and Water Research Institute, Nanyang Technological University, 1 Cleantech Loop, Singapore 637141, Singapore*
[e] *Department of Mechanical and Process Engineering, ETH Zurich, Leonhardstrasse 21, Zürich 8092, Switzerland*
[f] *Institute of Sustainability for Chemicals, Energy and Environment, Agency for Science, Technology and Research (A*STAR), 1 Pesek Road, Jurong Island, 627833, Singapore*
[g] *School of Materials Science and Engineering, Nanyang Technological University, Singapore 639798, Singapore*

† Electronic supplementary information (ESI) available: Determination of the oxygen non-stoichiometry, oxygen carrying capacity, weight loss curves during the N_2-TPD and isothermal TGA measurements under different p_{O2}. See DOI: https://doi.org/10.1039/d4cp02152e

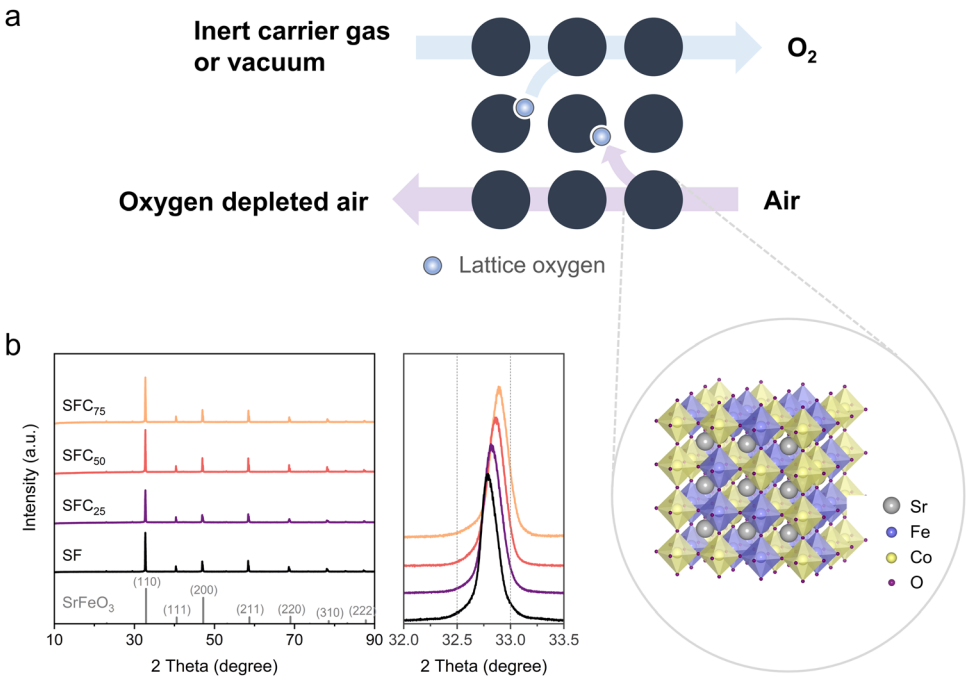

Fig. 1 (a) Schematic illustration of the chemical looping air separation (CLAS) process with Co-substituted $SrFeO_3$ perovskite as the oxygen carrier. (b) XRD patterns of the SF, SFC_{25}, SFC_{50}, and SFC_{75} perovskites, with a detailed scans around (110) diffraction peak. The reference $SrFeO_3$ pattern is obtained from JCPDS no. 39-0954.

CLAS relies on the redox reactions of oxide-based materials, also known as oxygen carriers, which can reversibly take up and release gaseous oxygen in response to variations in oxygen partial pressure and, or temperature. As illustrated by Fig. 1a, when the oxygen partial pressure is low, the lattice oxygen within the oxide is liberated in the form of gaseous oxygen, accompanied by the reduction of the oxide. The lattice oxygen in the reduced oxide is subsequently regenerated by put in contact with air. Repeating this cyclic process facilitates continuous air separation and oxygen production. The advantages of CLAS include high separation efficiency, low energy consumption, and the potential for integration with thermal power generation cycles, making it an attractive technology for potential industrial applications.[8–11]

Perovskite structured oxide materials have been extensively studied as potential oxygen carriers for CLAS owing to their unique structural and redox properties.[12–15] Perovskite structured oxides, with a general formula of ABO_3, are a class of materials in which A and B are cations of different ionic radii, while O represent oxygen anions. When the B-site cation undergoes redox reactions, the perovskites would take up or release oxygen based on the principle of charge balance, thereby facilitating CLAS.[16] Among the various perovskites structured oxide materials, strontium ferrite ($SrFeO_{3-\delta}$) has shown promising performance owing to its high oxygen capacity and excellent cyclability.[17] Indeed, the perovskite structured $SrFeO_{3-\delta}$, with δ ranging between 0 and 0.5, has drawn considerable scholarly interests in recent years for its application in CLAS and other chemical looping processes.[18–20] In addition, the abundant oxygen vacancies in $SrFeO_{3-\delta}$ based oxides afford excellent oxygen ion conductivity, rendering them excellent materials for oxygen permeation membranes.[21]

In $SrFeO_{3-\delta}$, the Fe ions exist in mixed valence states between +4 and +3 as the oxygen non-stoichiometry, δ varies between 0 and 0.5, where $\delta = 0.5$ signifies a substantial number of oxygen vacancies and a potential to undergo phase transformation to a brownmillerite structure (*i.e.* $Sr_2Fe_2O_5$). To further promote the oxygen release behavior of $SrFeO_{3-\delta}$, B-site substitution, *e.g.* by Co and Mn, has been explored.[22,23] Notably, B-site substitution by cobalt has been reported to modify the electronic structure of $SrFeO_{3-\delta}$, increase the oxygen desorption rate and lower the operating temperature of the CLAS process.[24] Fujishiro *et al.* conducted *in situ* X-ray absorption spectroscopy studies and have resolved the structural evolution of the $SrFe_{1-x}Co_xO_{3-\delta}$ perovskites when they undergo oxygen release at elevated temperatures. They found that the reduction of the Fe centers is primarily responsible for oxygen release.[22] Li and coworkers have conducted extensive investigation of A-site and B-site doped $SrFeO_3$ oxygen carriers and have identified (i) the net electronic charge of the oxygen anion,[25] (ii) the Gibbs free energy of formation of an oxygen vacancy[12] and (iii) the activation energy for oxygen diffusion and surface oxygen exchange[20] as energetic descriptors capable of predicting the CLAS activities of the perovskite material in terms of (a) the onset temperature for oxygen release and (b) the oxygen carrying capacities.

Building on the prior knowledge discussed above, we set out to further probe the origin of the variations in the oxygen release properties of B-site doped $SrFeO_3$ oxygen carriers, *viz.* $SrFe_{1-x}Co_xO_{3-\delta}$ (SFC), when they are subjected to CLAS cycles

under industrially relevant operating conditions (in the presence of high partial pressure of CO_2). Accordingly, a series of phase-pure perovskite samples with B site substitution by Co up to 75 mol%, *viz.* $SrFeO_{3-\delta}$ (SF), $SrFe_{0.75}Co_{0.25}O_{3-\delta}$ (SFC_{25}), $SrFe_{0.5}Co_{0.5}O_{3-\delta}$ (SFC_{50}), and $SrFe_{0.25}Co_{0.75}O_{3-\delta}$ (SFC_{75}) were synthesized *via* a sol–gel method. Temperature and oxygen partial pressure swing experiments, coupled with *in situ* structural, electronic characterizations, and *ab initio* simulations revealed the structural and electronic descriptors that gave rise to the improved CLAS performance of the SFC-based oxygen carriers.

2 Experimental section

2.1 Material preparation

The $SrFe_{1-x}Co_xO_{3-\delta}$ samples were prepared by sol–gel synthesis, which is widely employed for preparing perovskite-structured oxide powders and thin films.[26–29] $Sr(NO_3)_2$ (Sigma-Aldrich, 99.9%), $Fe(NO_3)_3{\cdot}9H_2O$ (Sigma-Aldrich, ≥98%), and $Co(NO_3)_2{\cdot}6H_2O$ (Sigma-Aldrich, 99%) were used as the metal precursors without any further purification. In a typical synthesis, stoichiometric amounts of metal nitrates (exact quantities given in Table S1, ESI†) were dissolved in 60 mL deionized water together with 5.845 g (20 mmol) of ethylenediaminetetraacetic acid (EDTA) and 7.685 g (40 mmol) of citric acid at room temperature. 100 mL of NH_4OH (30.0%) was used to adjust the pH to allow a clear solution to re-appear after mixing. Next, the solution was heated to 95 °C and held at 95 °C until a gel formed (*i.e.*, when the mixture is not visibly fluid). The gel was dried at 250 °C for 3 h in an oven and subsequently crushed to a fine powder. The powders were calcined in air at 1000 °C with a heating rate of 5 °C min^{-1} and a holding time of 5 h. The calcined powders were sieved to 100–200 μm for characterization and chemical looping air separation experiments.

2.2 Thermogravimetric analysis

A series of thermogravimetric analyses (TGA) were performed using a TGA/DSC2 (Mettler Toledo) thermogravimetric analyzer to investigate the relationship between the temperature (T), oxygen partial pressure (p_{O_2}), oxygen stoichiometry ($3-\delta$), and oxygen carrier compositions (x). The absolute δ value of the as-synthesized perovskite oxygen carriers was first determined by temperature programed desorption (TPD) experiment, in which 50 mg of the sample was heated from 150 °C to 1000 °C at a rate of 5 °C min^{-1} in a N_2 flow (200 mL min^{-1}). This program allowed the perovskite phase to be fully reduced to brownmillerite ($SrFe_{1-x}Co_xO_{2.5}$, δ = 0.5).[30] The mass change (Δm) between 150 °C in air and 1000 °C in N_2 was measured. This mass change corresponds to the loss of lattice oxygen in the perovskite structure (*i.e.*, a change in δ) prior to phase transition to brownmillerite. Subsequently, the value of δ_0 at 150 °C in air was calculated using the following equation, assuming δ = 0.5 at 1000 °C in N_2:

$$\Delta m/m = (0.5 - \delta_0)M_O/M_S \quad (1)$$

where Δm is the change in sample mass; m is the initial sample mass at 150 °C; M_O is the atomic mass of oxygen; M_S is the molar mass of the sample at its initial state. With the δ_0 known at the reference state (T = 150 °C, p_{O_2} = 0.2 bar), δ at any given T and p_{O_2} could be determined according to:

$$\Delta m/m = (\delta - \delta_0)M_O/M_S \quad (2)$$

In a typical TGA experiment, 50 mg of sample was placed in an alumina crucible (150 μL), heated to 150 °C at a rate of 5 °C min^{-1} and held for 30 min in air. After the isothermal period, p_{O_2} was changed to 0.2 bar, 0.1 bar, 0.05 bar, or 0.02 bar by using either air or a N_2/air mixture of. Then, the sample was heated from 250 °C to 650 °C in increments of 50 °C, and held at each incremental temperature for 30 min to investigate the relationship between T, p_{O_2}, δ, and x for each sample when it is in equilibrium with the gas. The total gas flow over the microbalance was maintained at 200 mL min^{-1} (measured at room temperature and pressure) throughout the experiment.

2.3 Material characterization

The oxygen contents of the as-synthesized oxygen carriers were quantified by iodometric titration. In a typical titration experiment, a perovskite sample weighing 250 mg was dissolved in 50 mL of 6 M HCl. Subsequently, 10 mL of this solution was transferred into an Erlenmeyer flask, to which 1.00 g of potassium iodide (KI) was introduced. A few minutes later, the solution was diluted with deionized (DI) water and the released iodine was titrated using 0.05 M sodium thiosulfate ($Na_2S_2O_3$). Prior to each titration, sodium thiosulfate was standardized against potassium iodate (KIO_3). The titration endpoint was identified using a starch indicator, which was added into the solution prior to the titration.

The morphologies of the samples were examined by a field emission scanning electron microscope with equipped with energy dispersive spectroscopy (JEOL JSM-7200F). The crystal structures of the as-prepared oxygen carriers were studied by powder X-ray diffraction (XRD) in a Bruker D8 Advance diffractometer with filtered Cu Kα radiation (λ = 1.5418 Å) at 40 kV and 40 mA under ambient condition. The XRD patterns were collected with 2θ range from 10° to 90°, a step size of 0.02°, and a collection time of 1 s per step. In addition, *in situ* XRD experiments were conducted to monitor the structural changes of the perovskite oxygen carriers over a CLAS cycle. In the first *in situ* XRD experiment, the sample was heated up in air at 10 °C min^{-1} to 100, 200, 300, 400, and 500 °C, consecutively, dwelling for 2 h at each temperature, followed by a 2 h scan for 2θ = 10–90° at that temperature before heating up to the next set point temperature. After the scan at 500 °C, the sample was cooled down consecutively to 400, 300, 200, and 100 °C, while following the same temperature dwelling and XRD scanning program. In the second *in situ* XRD experiment, a fresh sample was first heated up in air stepwise to 100, 200, 300, 400, 500 °C, consecutively, with a pattern collected over the 2θ range of 30–35° at each temperature point before cooling down. Then, the same temperature-XRD program was repeated in a 1 : 1

mixture of air and CO_2. The XRD data collected were analyzed by Rietveld refinement using GSAS software through EXPGUI.[31]

2.4 Density functional theory (DFT) calculation

Density of states (DOS) of the oxygen carriers were obtained by DFT computation using the Vienna ab initio simulation package (VASP) software[32,33] with the projector-augmented wave (PAW) approach[34] and the Perdew–Burk–Ernzerhof (PBE) exchange–correlation functional.[32,33,35] To account for the strongly localized d-electrons, effective Hubbard U parameters for Fe and Co are set to be 4.0 and 3.3 eV, respectively, taken from the literature.[36] Structural models used for the calculation were $2 \times 2 \times 2$ cubic perovskite supercells with various extent of B-site substitution. The Brillouin zone was sampled in a $6 \times 6 \times 6$ mesh, and the plane-wave cut-off energy was set to be 520 eV.

3 Results and discussion

3.1 Characterization of oxygen carriers

The crystal structures of the as-prepared perovskite oxygen carriers were studied by powder X-ray diffraction (XRD). The undoped $SrFeO_{3-\delta}$ (SF) and Co-doped SFC all showed cubic-phase perovskite structures (with $Pm3m$ space group), with major peaks at 32.8, 40.4, 47.0, 58.5, 68.7, and 78.2°, indexed to (110), (111), (200), (211), (220), and (310) reflections, respectively (Fig. 1b). Accordingly, the $Pm3m$ space group was used as a reference structure for analyzing the data collected by the *in situ* XRD experiments following Rietveld refinement. The results of the Rietveld refinement, including lattice constant, crystallite size, dislocation density,[37] and microstrain, are summarized in Table S4 (ESI†). These structural parameters are known to influence the properties of perovskite-structured materials.[15,38–40] From the XRD results, no impurity phase was detected, verifying the successful synthesis of phase-pure, perovskite structured, Co-doped $SrFeO_{3-\delta}$, even at a Co occupancy as high as 75% (*i.e.*, 25% Fe occupancy). Little or no sign of lattice distortion could be observed from the refinement results, whereas the microstrain of the perovskite structure appears slightly increased upon Co doping. A clear shift of diffraction peaks to higher 2θ is observed with increasing Co content. This indicates Co cations are well-confined in the B sites, substituting Fe, leading to lattice contraction as a result of the relatively small radii of Co^{4+} and Co^{3+} ions *cf.* the Fe^{4+} and Fe^{3+} ions. This trend is also corroborated by the quantitative analysis of the refined XRD pattern shown in Table S4 (ESI†). Therefore, despite the different extent of Co doping, the lattice structure of the $SrFe_{1-x}Co_xO_{3-\delta}$ closely resembles that of the undoped $SrFeO_{3-\delta}$.

The sample morphology and elemental homogeneity at the microscopic level were analyzed using SEM and EDS mapping. As shown in Fig. 2, a uniform dispersion of all constituent elements could be confirmed, without any observation of agglomeration, locally high concentration, or impurity phases. The SF and SFC oxygen carrier particles were observed to have porous surfaces, which are beneficial for rapid oxygen uptake and release during CLAS.

Even in ambient air, $SrFeO_3$ and its Co-doped variants can have oxygen non-stoichiometry. Therefore, the oxygen non-stoichiometries (*i.e.*, δ) of the oxygen carriers were first determined prior to any further evaluation, by both iodometric titration and temperature programed desorption (TPD). The results of the latter analysis are discussed in the next section. As shown in Table S2 (ESI†), the $(3-\delta)$ value of the as-prepared

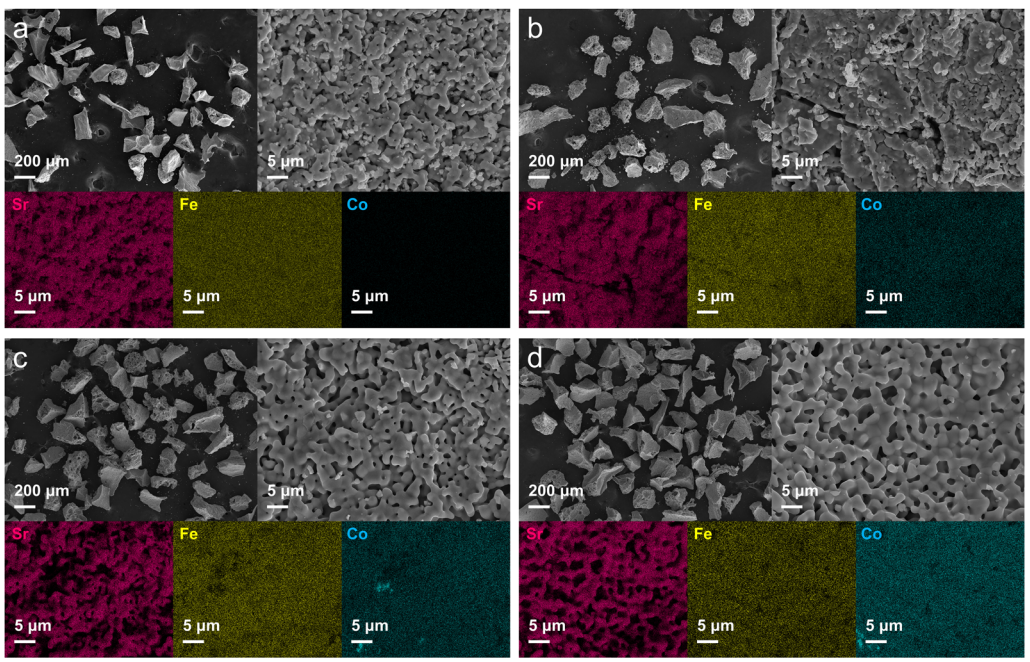

Fig. 2 SEM and EDX mappings of the as-prepared (a) SF, (b) SFC_{25}, (c) SFC_{50}, and (d) SFC_{75} perovskite oxygen carriers.

oxygen carriers in air was found to decrease systematically from 2.83 to 2.68 as Co ratio (x) increase from 0 to 0.75. The values obtained here are similar to those determined in the literature for $SrFe_{1-x}Co_xO_{3-\delta}$ prepared by sol–gel methods.[41,42]

3.2 Oxygen uptake and release through temperature swings

The temperature programed oxygen release experiments were first conducted in nitrogen to validate the oxygen content estimated by iodometric titration, as well as to reveal the change in the activity of oxygen carriers induced by Co-substitution. The complete decomposition of perovskite resulted in a phase transformation to $SrFe_{1-x}Co_xO_{2.5}$ brownmillerite.[43] The weight loss curves (see Fig. S1, ESI†) during this process were collected to determine the initial oxygen content, $3-\delta_0$. In the N_2-TPD profiles, SFC was found to lose less weight than undoped SF, suggesting its initial oxygen content is closer to that of brownmillerite (2.5). As summarized in Table S2 (ESI†), the results derived from N_2-TPD are in close agreement with those obtained by iodometric titration, with higher Co occupancy (x) corresponding to greater oxygen non-stoichiometry.

The effect of Co doping could be clearly observed from the N_2-TPD profiles. As shown in Fig. 3a, the SFC perovskites tend to lose weight at lower temperatures than the undoped SF. For SF, the onset temperature for O_2 release was around 400 °C. After Co doping, the onset temperature as well as the peak temperature for oxygen release shift to increasingly lower temperatures with increasing Co occupancy, indicating higher activity for oxygen release. Here, the onset temperature for oxygen release was defined as the temperature at which the oxygen carriers started to lose weight. In general, the enhancement in oxygen release activity is more profound for samples with more Co doping. For SFC_{75}, oxygen release started at a temperature as low as 300 °C. Air-TPD have also been conducted, as summarized in Fig. 3b. Although the heating rate appears to influence the onset temperature, especially when the heating rate is high, the promotional effect of Co-doping is ubiquitous at all heating rates (1, 3, 5 and 10 °C min^{-1}). SFC_{75} exhibited an onset temperature ~100 °C lower than that of SF, indicating that the promotional effect of Co doping is applicable across a wide range of oxygen partial pressure (*i.e.*, any mixture of N_2 and air).

TGA experiments across a wide range of temperatures (T) and oxygen partial pressures (p_{O_2}) were conducted to systematically investigate the oxygen uptake-release behavior of the SF and SFC oxygen carriers. In the isothermal experiments (detailed program shown in Fig. S2a, ESI†), oxygen carrier samples were subjected to a specified p_{O_2} (between 0.02 and 0.2 bar) under elevated temperature (150–650 °C). As shown in Fig. S2b (ESI†), under each p_{O_2}, SFC_{75} started losing weight at the lowest temperature amongst all samples. All perovskite oxygen carriers exhibited fast oxygen release behavior, as indicated by the observation that the sample mass quickly equilibrated to a steady value upon reaching a new temperature set point, as shown Fig. S2b (ESI†). At each time point (*i.e.*, under the same T and p_{O_2}), the mass change of the oxygen carriers followed the trend of $SFC_{75} > SFC_{50} > SFC_{25} > SF$, indicating that the SFC_{75} possesses the highest oxygen carrying capacity for any given temperature swing.

The oxygen stoichiometry ($3-\delta$) and oxygen carrying capacity (with reference to T = 150 °C and p_{O_2} = 0.2 bar) were determined according to eqn (2). In general, a lower oxygen partial pressure corresponds to a lower ($3-\delta$) value. At p_{O_2} = 0.2 bar, the $3-\delta$ values approach 2.5 (δ = 0.5) when the temperature is above 500 °C, indicating the tendency of phase change from perovskite to brownmillerite. While the value of ($3-\delta$) could be reduced below 2.5 under highly reducing conditions (*e.g.* $T > 800$ °C, $\log(p_{O_2}) < -3$), such conditions are not applicable to CLAS processes.[38] The capacity of these perovskite oxygen carriers for CLAS applications could be further evaluated by analyzing the oxygen carrying capacities. As expected, all perovskite-structured oxygen carriers release more gaseous oxygen when exposed to higher temperatures. As shown in Fig. 4, SFC_{75} was found to possess the highest oxygen carrying capacity amongst all oxygen carriers, especially in the temperature range above 400 °C. Under the condition of T = 650 °C and p_{O_2} = 0.02 bar, SFC_{75} shows an oxygen carrying capacity of ~1.5 wt%, *i.e.* a ~20% improvement compared to undoped SF. In summary, the results from

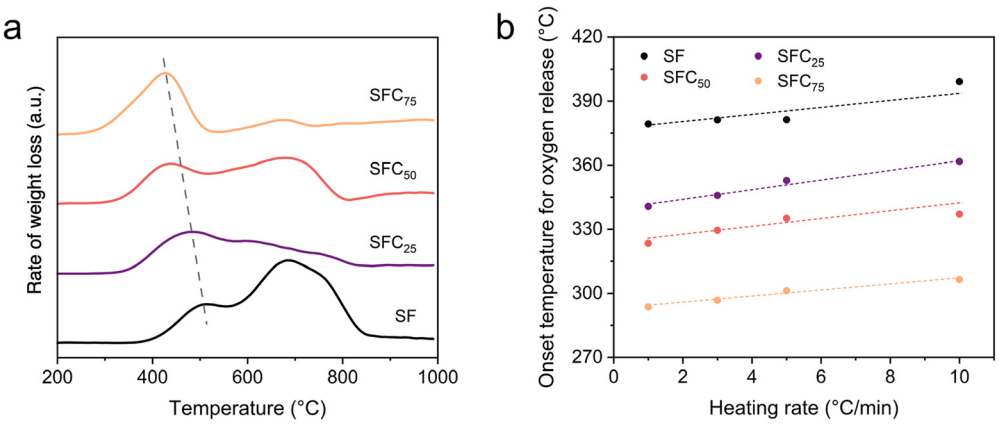

Fig. 3 Temperature-programmed oxygen desorption profiles of the perovskite oxygen carriers in (a) N_2 and (b) air. There N_2-TPD profiles (derivative weight) were derived from the weight loss curves shown in Fig. S1 (ESI†).

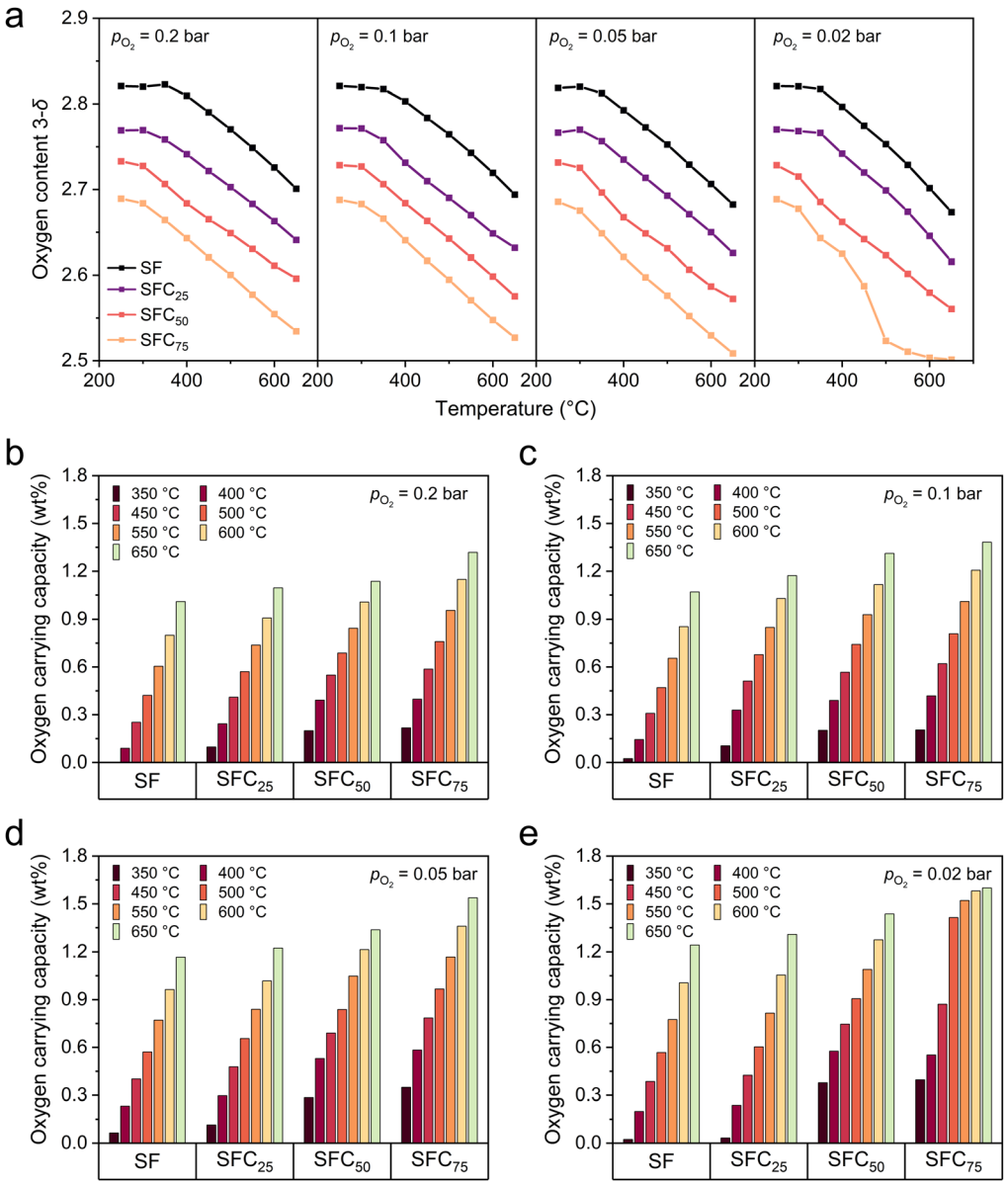

Fig. 4 (a) Oxygen non-stoichiometry and (b)–(e) oxygen carrying capacity of the $SrFe_{1-x}Co_xO_{3-\delta}$ perovskite oxygen carriers as a function of T, p_{O_2}, and x. Reference state for the determination of oxygen carrying capacity: T = 150 °C and p_{O_2} = 0.2 bar.

isothermal experiments under various oxygen partial pressure have confirmed the enhanced CLAS performance of the Co-doped SF perovskites.

The stability of the crystal structure of the perovskite oxygen carriers is essential to ensuring cyclic durability, since it will undergo cyclic phase changes upon oxygen release and uptake. Accordingly, the structural changes of the oxygen carriers were investigated by *in situ* XRD. During the temperature excursion from 100 °C to 500 °C and back, the refined *in situ* XRD data indicate that all SF and SFC oxygen carriers were able to fully restore their original lattice structures and lattice parameters (Fig. 5a), suggesting excellent structural reversibility and cyclic stability. Then, the perovskite samples were subjected to temperature cycles in air and a 1 : 1 air/CO_2 mixture (temperature program shown in Fig. 5b). As shown by the *in situ* diffractograms in Fig. 5c, as the O_2 release progressed with temperature increase (*i.e.*, as the scan number increased), the characteristic (110) diffraction peak shifted towards smaller angles, indicative of an expanding perovskite unit cell due to thermal expansion accompanied by the depletion of lattice oxygen. Upon cooling back to room temperature, the diffraction peak restored its initial position, demonstrating reversibility and thermal stability over the redox process. Moreover, the same experiment conducted in a 1 : 1 air/CO_2 mixture revealed a shift in the main perovskite peak (110) to lower angles, signifying further O_2 release. This is expected as the degree of oxygen release increases with decreasing oxygen partial pressure. At the same time, the *in situ* XRD patterns in air/CO_2 have

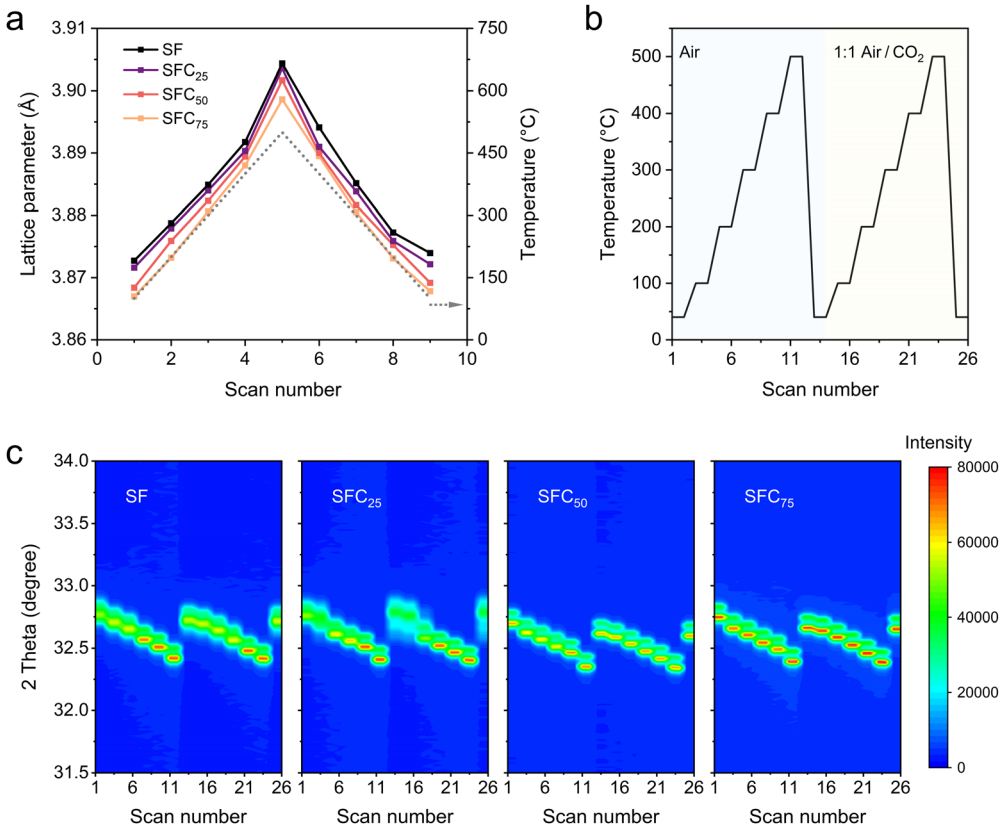

Fig. 5 Results of the *in situ* XRD experiments. (a) Refined lattice parameters of perovskite oxygen carriers at different temperatures during the first temperature excursion in air. (b) Experimental conditions of the second and the third temperature excursions. (c) XRD patterns collected in the (110) region during the second and third temperature excursions, when the samples were exposed to air and 1 : 1 air/CO_2, respectively (round 2).

shown no evidence of carbonate phase formation, which would be detrimental to the performance of the perovskite materials, especially because Sr-containing perovskites are known to undergo carbonation in CO_2 to form $SrCO_3$.[44] The resistance to carbonation assumes critical importance, especially in processes such as CLAS or oxyfuel combustion, the oxygen release could take place in highly concentrated CO_2. Consequently, materials suffering severely from carbonation are unsuitable for CLAS.[45] In summary, the *in situ* XRD experiments corroborates the feasibility of employing the SF and SFCs for CLAS applications using CO_2 as a carrier gas, which is relevant to processes such as oxy-fuel combustion and Allam cycle.

The cyclic durability of the perovskite oxygen carriers was examined by isothermal redox swing cycles (*i.e.*, switching between air and N_2) at 500 °C. Each cycle consists of a 10 min oxidation stage in air, followed by a 30 min reduction stage in N_2. For all samples, the cyclic mass changes have stabilized after the fifth cycle and became highly reproducible for the remaining 45 cycles (Fig. 6). In other words, all the SF and SFC perovskite oxygen carriers have shown excellent cyclic stability. Amongst all the samples, SFC_{75} has shown the highest oxygen carrying capacity of ~1.3 wt%, whereas the undoped SF only have a capacity of ~0.5 wt%, signifying the apparent benefit of Co doping. It could also be observed from the detailed weight loss curve during cycles 2–3 (Fig. 6e) and cycles 49–50 (Fig. 6f) that the SFC_{75} exhibited superior redox kinetics, with almost identical apparent rate of oxygen uptake and significantly faster apparent rate of oxygen release than all other samples; both rates remain unchanged over 50 cycles. Upon completion of the extended cycling experiment, the morphology of the spent oxygen carriers was characterized by SEM, as shown in Fig. 7. Remarkably, the morphologies of all the perovskite oxygen carrier particles remained nearly unchanged, with the porous surface morphology well preserved after 50 redox cycles. Therefore, the results above showed the suitability of SF and SFC oxygen carriers for CLAS up to 500 °C, without inducing any irreversible or undesirable (*i.e.*, transformation from perovskite to brownmillerite) change in phase composition or morphology.

3.3 *Ab initio* rationalization of oxygen carrier performance

Several structural descriptors, derived from *ab initio* calculations, were investigated in order to probe the composition-structure–function relationship of the B-site substituted SFC perovskites for CLAS applications. For perovskite materials, the Goldschmidt tolerance factor may be used as a simple descriptor of the perovskite's stability and is often used to describe the perceived activity of doped perovskite phases:[46]

$$t = \frac{r_{Sr} + r_O}{\sqrt{2}([r_{Co}x + r_{Fe}(1-x)] + r_O)} \quad (3)$$

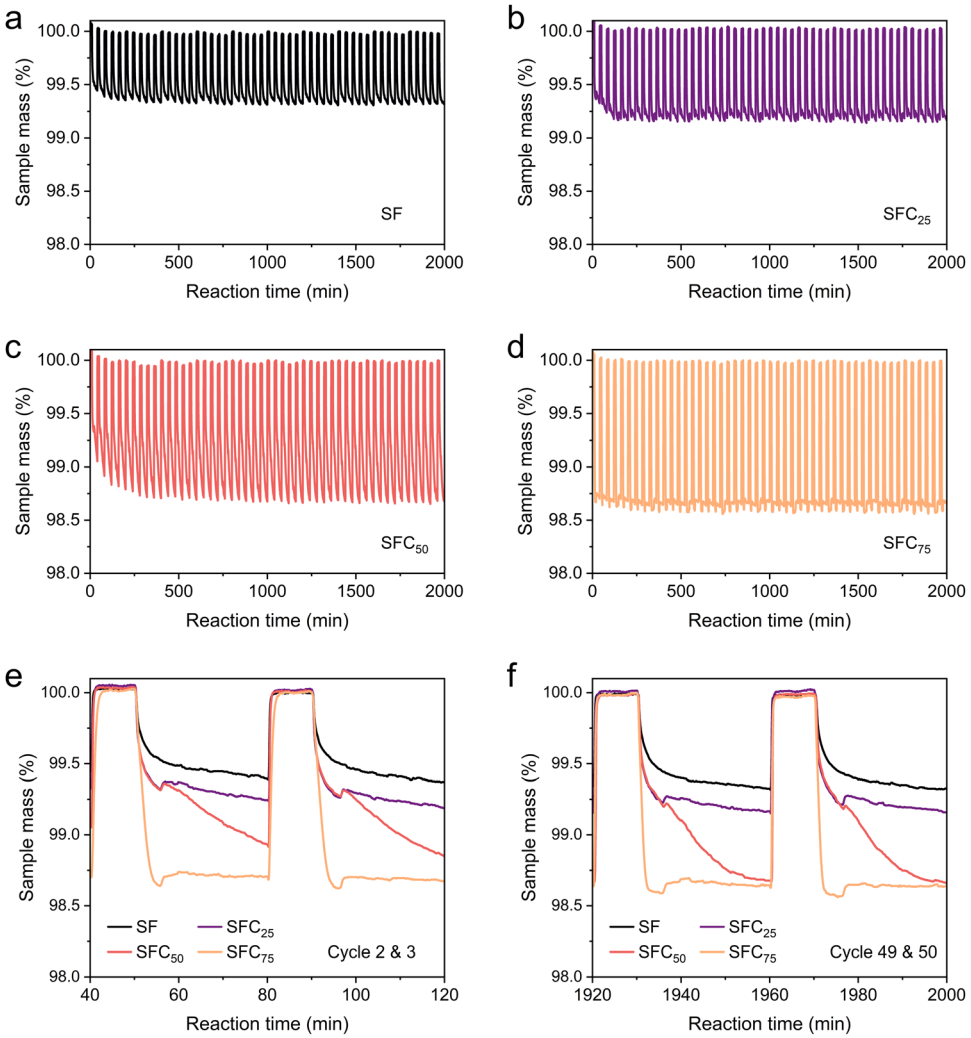

Fig. 6 Weight change curves for (a) SF, (b) SFC_{25}, (c) SFC_{50}, and (d) SFC_{75} oxygen carriers during 50 redox swing cycles between air and N_2 at 500 °C. Detailed comparisons of weight loss curves are shown for (e) cycles 2–3 and (f) cycles 49–50.

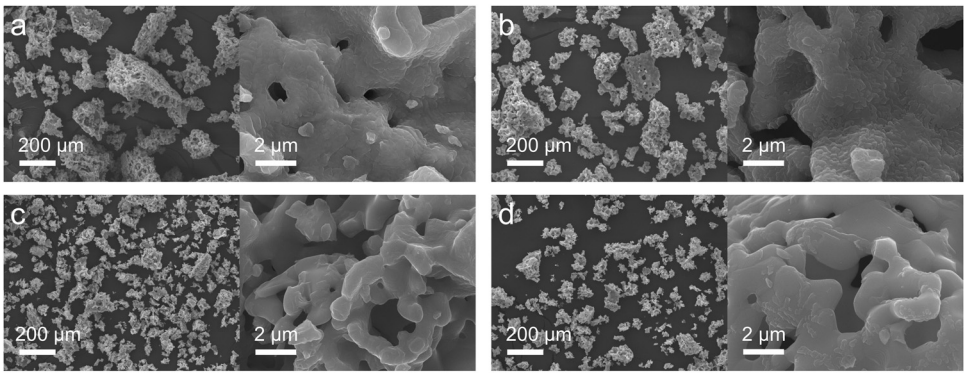

Fig. 7 SEM images of the (a) SF, (b) SFC_{25}, (c) SFC_{50}, and (d) SFC_{75} perovskites after 50 TGA cycles.

where r_{Sr}, r_{Co}, r_{Fe} and r_O are the radii of the Sr, Co, Fe, and O ions, respectively.[47] The parameter x corresponds to the fractional occupancy of the B site. An undistorted, perfect cubic perovskite lattice possesses a tolerance factor of 1.00. Deviations from t = 1 lead to distortions in the perovskite lattice structure.[48] Excessive distortions could result in phase transformations and the emergence of phases other than perovskite or its lower-symmetry variants. The gradual replacement of Fe^{4+} (r = 0.585 Å) occupying

Table 1 Structural descriptors of oxygen carriers: tolerance factor (t), O 2p band center (ε_{2p}), and transition metal–oxygen (TM–O) hybridization intensity

Oxygen carrier	Tolerance factor	O 2p band center (eV)	Hybridization intensity (%)
SF	1.019	−1.951	32.98
SFC_{25}	1.027	−1.948	37.29
SFC_{50}	1.034	−1.902	44.32
SFC_{75}	1.042	−1.887	51.29

the octahedral centres with Co^{4+} (r = 0.530 Å) cations in SFC leads to an increase in the tolerance factor from 1.019 to 1.042, as summarized in Table 1. This, in turn, results in a slightly less stable perovskite structure, which is more prone to decomposition and oxygen release, in line with experimental observations and XRD refinement results. Therefore, the results suggest that the tolerance factor could be a suitable descriptor for predicting and modulating the lattice oxygen activity in mixed perovskite materials for CLAS applications. To validate the correlation between the structural descriptors and the experimentally observed activity for CLAS, the onset temperature for oxygen release in air at a heating rate of 1 °C min^{-1} and the oxygen carrying capacity obtained at the 50th cycle of the pressure swing experiments were used as the experimental performance descriptors, similar to previous work.[12,13,20,25] As plotted in Fig. 9, an obvious correlation between the tolerance factor and the onset temperature as well as oxygen carrying capacity could be observed, revealing the applicability of tolerance factor for predicting the CLAS activity of the SF and SFC oxygen carriers.

Besides crystal structure parameters, B-site substitution can alter the electronic structures of the perovskites and changes the chemical activities of the perovskites, both in terms of thermodynamics and kinetics. Here, density functional theory (DFT) calculations were carried out to analyze the electronic structures of SF, SFC_{25}, SFC_{50}, and SFC_{75} perovskite oxygen carriers. Fig. S3 (ESI†) shows the calculated partial density of state (DOS) plots of the 3d orbitals of the transition metals (*viz.* Fe and Co) and the O 2p orbitals. For all perovskite samples, the DOS at the Fermi energy (E_F) is, with the band gap being less than 2 eV, *i.e.*, these Fe-based perovskite are semiconductors. It could be noticed that the Fe 3d band become less intense while the Co 3d band intensifies with increasing the Co content in the SFC. Besides, the valence band near the Fermi level is primarily occupied by O 2p states, while the conduction band (unoccupied states above E_F) is mainly dominated by Fe 3d states. The above observations are in agreement with previous studies.[25,49] The relationship between the O 2p-band center and transition metal–oxygen interaction in perovskite structures is often considered important to the redox activities of transition metal oxide catalysts.[50] Here, the O 2p-band center (ε_{2p}) is defined as:

$$\varepsilon_{2p} = \frac{\int E \cdot D(E - E_F)\mathrm{d}E}{\int D(E - E_F)\mathrm{d}E} \quad (4)$$

where $D(E)$ denotes the projected density of states (PDOS) of the O 2p band, and E_F is the Fermi level energy. The calculated O 2p band centers are summarized in Table 1. Typically, a higher O 2p-band center (against Fermi level) indicates greater covalency, which is more beneficial for oxygen release.[25] To validate the effectiveness of using O 2p-band center as a structural descriptor, the relationship between ε_{2p} and the experimental descriptors are examined. As shown in Fig. 9, the position of the O 2p-band center relative to the Fermi level negatively correlates to the onset oxygen release temperature, and positively correlate with the oxygen carrying capacity. Therefore, the design of perovskite materials for CLAS should target achieving a higher O 2p center through doping and structural modulation.

The degree of hybridization between O 2p and TM 3d states is also proposed to represent the nature of metal–oxygen interaction, and subsequently the redox activity of metal oxides.[51,52] Fig. 8 illustrates the hybridization between O 2p and TM 3d states of SFC_{75}. Here, the degree of hybridization is estimated by quantifying the overlap between the TM 3d and O 2p bands (annotated in purple in Fig. 8), calculated according:

$$\text{Hybridization intensity} = \text{PDOS (O 2p)}_{\text{overlapped}}/\text{PDOS (O 2p)} \quad (5)$$

The results of hybridization of the various perovskite structured oxygen carriers are summarized in Table 1. As depicted in Fig. 9, there is a strongly negative correlation between the degree of hybridization and the onset temperature for oxygen release. In fact, the onset temperature for oxygen release shows apparently greater correlation with the degree of hybridization than the O 2p center as descriptors. In prior studies, the relationships between the CLAS performance of substituted strontium ferrite perovskites oxygen carriers and other DFT calculated descriptors, such as energy for oxygen vacancy formation and net electronic charge have also been reported.[12,25] Accordingly, the findings in the present study offer further insights into the electronic origins of the activity perturbation by B-site substitution.

Besides B-site substitution, further studies on A-site substitution as well as other substitutional B-site dopants are also

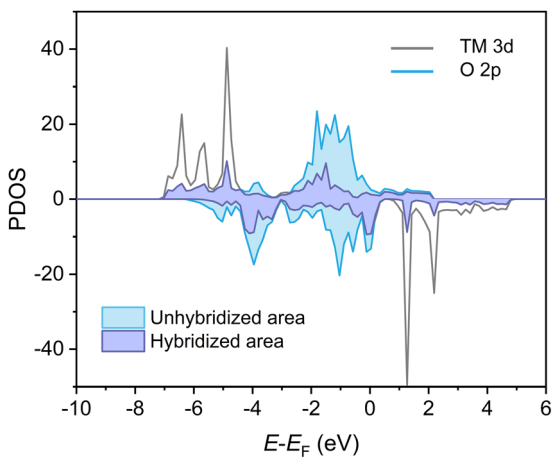

Fig. 8 Illustration of hybridization between the O 2p states and TM 3d states of SFC_{75}.

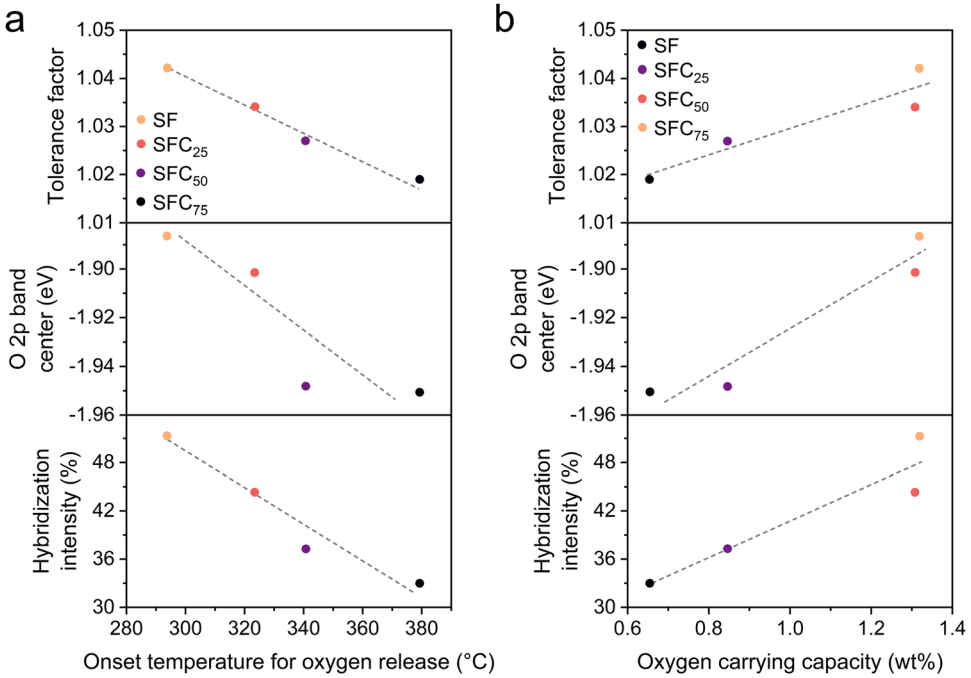

Fig. 9 Correlation between the structural descriptors and the performance of oxygen carriers: (a) onset temperature for oxygen release and (b) oxygen carrying capacity. Onset temperature data are taken from the TPD experiment in air with a heating rate of 1 °C min^{-1}, and oxygen carrying capacity data are taken from the pressure swing experiments at the 50th cycle.

worthwhile, particularly for validating the applicability of the descriptors discussed in the present study, including tolerance factor, O 2p-band center, and the degree of TM–O hybridization. In addition, future simulation work should also investigate the release of gaseous oxygen by perovskite structured oxides with existing oxygen vacancies.

4 Conclusions

In this study, the consequence of Co substitution at the B sites of $SrFeO_3$ is systematically investigated for the application of CLAS. Phase-pure perovskites with B-site Co substitution up to 75% was prepared by a sol–gel method. Thermogravimetric analysis revealed that the oxygen uptake and release performance of the strontium ferrite-based perovskite materials, characterized by onset temperature for oxygen release and oxygen carrying capacity, can be effectively altered through B-site substitutional doping. All the perovskite structured oxygen carriers, including SF and SFC, showed excellent cyclic stability over pressure swing (air-N_2) cycles at 500 °C, suggesting their suitability for long-term CLAS operation. Deactivation due to carbonation of Sr is generally absent in the presence of CO_2 in the process stream. The experimental observations can be rationalized by the enhanced activity of the TM–O bonds, which can originate from structural perturbation as characterized by the Goldschmidt tolerance factor, as well as changes in the electronic structure as characterized by the O 2p center and the degree of TM–O hybridization. These correlations offer *ab initio* rationales for designing high-performance perovskite-structured oxygen carriers for CLAS and other chemical looping applications through hypothesis-driven synthesis.

Data availability

Data for this article, including empirical data (*e.g.* tabular files, text files, images, *etc.*) are available at NTU Research Data Repository at **https://doi.org/10.21979/N9/OGIWAS**.

Conflicts of interest

The authors declare no competing financial interest.

Acknowledgements

The authors would like to thank the financial support by Ministry of Education Singapore's Academic Research Fund Tier 1 (RT03/19 and RG112/18) and the National Research Foundation (NRF), Prime Minister's Office, Singapore under its Campus for Research Excellence and Technological Enterprise (CREATE) programme.

References

1 K. Shah, B. Moghtaderi and T. Wall, *Energy Fuels*, 2012, **26**, 2038–2045.
2 F. Wu, M. D. Argyle, P. A. Dellenback and M. Fan, *Prog. Energy Combust. Sci.*, 2018, **67**, 188–205.

3 A. R. Smith and J. Klosek, *Fuel Process. Technol.*, 2001, **70**, 115–134.
4 W. Castle, *Int. J. Refrig.*, 2002, **25**, 158–172.
5 R. S. Murali, T. Sankarshana and S. Sridhar, *Sep. Purif. Rev.*, 2013, **42**, 130–186.
6 N. F. Himma, A. K. Wardani, N. Prasetya, P. T. Aryanti and I. G. Wenten, *Rev. Chem. Eng.*, 2019, **35**, 591–625.
7 Q. Imtiaz, D. Hosseini and C. R. Müller, *Energy Technol.*, 2013, **1**, 633–647.
8 Z. Deng, B. Jin, Y. Zhao, H. Gao, Y. Huang, X. Luo and Z. Liang, *Energy Convers. Manage.*, 2018, **160**, 289–301.
9 C. Zhou, K. Shah, H. Song, J. Zanganeh, E. Doroodchi and B. Moghtaderi, *Energy Fuels*, 2016, **30**, 1741–1755.
10 S. Saqline, H. Wang, Q. Fan, F. Donat, C. Müller and W. Liu, *Appl. Energy Combust. Sci.*, 2024, **17**, 100238.
11 S. Saqline, L. Yang, A. Romagnoli and W. Liu, *J. Cleaner Prod.*, 2023, **418**, 138097.
12 E. Krzystowczyk, X. Wang, J. Dou, V. Haribal and F. Li, *Phys. Chem. Chem. Phys.*, 2020, **22**, 8924–8932.
13 J. Dou, E. Krzystowczyk, X. Wang, A. R. Richard, T. Robbins and F. Li, *J. Phys.: Energy*, 2020, **2**, 025007.
14 E. Krzystowczyk, V. Haribal, J. Dou and F. Li, *ACS Sustainable Chem. Eng.*, 2021, **9**, 12185–12195.
15 H. Kusaba, G. Sakai, K. Shimanoe, N. Miura and N. Yamazoe, *Solid State Ionics*, 2002, **152–153**, 689–694.
16 J. Vieten, B. Bulfin, F. Call, M. Lange, M. Schmucker, A. Francke, M. Roeb and C. Sattler, *J. Mater. Chem. A*, 2016, **4**, 13652–13659.
17 B. Bulfin, J. Lapp, S. Richter, D. Gubàn, J. Vieten, S. Brendelberger, M. Roeb and C. Sattler, *Chem. Eng. Sci.*, 2019, **203**, 68–75.
18 E. Marek, W. T. Hu, M. Gaultois, C. P. Grey and S. A. Scott, *Appl. Energy*, 2018, **223**, 369–382.
19 R. H. Görke, E. J. Marek, F. Donat and S. A. Scott, *Int. J. Greenhouse Gas Control*, 2020, **94**, 102891.
20 J. Dou, E. Krzystowczyk, X. Wang, T. Robbins, L. Ma, X. Liu and F. Li, *ChemSusChem*, 2020, **13**, 385–393.
21 Y. Hayamizu, M. Kato and H. Takamura, *J. Membr. Sci.*, 2014, **462**, 147–152.
22 F. Fujishiro, N. Oshima, T. Sakuragi and M. Oishi, *J. Solid State Chem.*, 2022, **312**, 123254.
23 F. Fujishiro, N. Oshima, N. Kamioka, T. Sakuragi and M. Oishi, *J. Solid State Chem.*, 2020, **283**, 121152.
24 G. Luongo, F. Donat and C. R. Müller, *Phys. Chem. Chem. Phys.*, 2020, **22**, 9272–9282.
25 X. Wang, E. Krzystowczyk, J. Dou and F. Li, *Chem. Mater.*, 2021, **33**, 2446–2456.
26 F. Mikailzade, F. Önal, M. Maksutoglu, M. Zarbali and A. Göktaş, *J. Supercond. Novel Magn.*, 2018, **31**, 4141–4145.
27 A. Goktas, I. H. Mutlu and A. Kawashi, *Thin Solid Films*, 2012, **520**, 6138–6144.
28 H. Gencer, A. Goktas, M. Gunes, H. I. Mutlu and S. Atalay, *Int. J. Mod. Phys. B*, 2008, **22**, 497–506.
29 H. Gencer, M. Gunes, A. Goktas, Y. Babur, H. I. Mutlu and S. Atalay, *J. Alloys Compd.*, 2008, **465**, 20–23.
30 M. Schmidt, *J. Phys. Chem. Solids*, 2000, **61**, 1363–1365.
31 B. H. Toby, *J. Appl. Crystallogr.*, 2001, **34**, 210–213.
32 G. Kresse and J. Furthmüller, *Phys. Rev. B: Condens. Matter Mater. Phys.*, 1996, **54**, 11169–11186.
33 G. Kresse and J. Hafner, *Phys. Rev. B: Condens. Matter Mater. Phys.*, 1993, **47**, 558–561.
34 P. E. Blöchl, *Phys. Rev. B: Condens. Matter Mater. Phys.*, 1994, **50**, 17953–17979.
35 J. P. Perdew, K. Burke and M. Ernzerhof, *Phys. Rev. Lett.*, 1996, **77**, 3865–3868.
36 Y.-L. Lee, J. Kleis, J. Rossmeisl, Y. Shao-Horn and D. Morgan, *Energy Environ. Sci.*, 2011, **4**, 3966–3970.
37 L. K. Parmar, R. Joshi, P. Yadav, T. Garg, A. Kumar and A. Yadav, *Chem. Phys. Impact*, 2024, **8**, 100603.
38 A. Holt, T. Norby and R. Glenne, *Ionics*, 1999, **5**, 434–443.
39 J. P. Hodges, S. Short, J. D. Jorgensen, X. Xiong, B. Dabrowski, S. M. Mini and C. W. Kimball, *J. Solid State Chem.*, 2000, **151**, 190–209.
40 A. Göktaş, A. Tumbul and F. Aslan, *J. Sol-Gel Sci. Technol.*, 2016, **78**, 262–269.
41 L. Kokhanovskii, V. Vashuk, O. Ol'shevskaya and O. Kirilenko, *Inorg. Mater.*, 2001, **37**, 730–736.
42 I. Starkov, S. Bychkov, A. Matvienko and A. Nemudry, *Phys. Chem. Chem. Phys.*, 2014, **16**, 5527–5535.
43 V. L. Kozhevnikov, I. A. Leonidov, M. V. Patrakeev, E. B. Mitberg and K. R. Poeppelmeier, *J. Solid State Chem.*, 2001, **158**, 320–326.
44 V. Kharton, A. Yaremchenko, A. Kovalevsky, A. Viskup, E. Naumovich and P. Kerko, *J. Membr. Sci.*, 1999, **163**, 307–317.
45 C. Y. Lau, M. T. Dunstan, W. Hu, C. P. Grey and S. A. Scott, *Energy Environ. Sci.*, 2017, **10**, 818–831.
46 J. Vieten, B. Bulfin, P. Huck, M. Horton, D. Guban, L. Zhu, Y. Lu, K. A. Persson, M. Roeb and C. Sattler, *Energy Environ. Sci.*, 2019, **12**, 1369–1384.
47 R. D. Shannon, *Acta Crystallogr., Sect. A: Cryst. Phys., Diffr., Theor. Gen. Crystallogr.*, 1976, **32**, 751–767.
48 W. T. Hong, M. Risch, K. A. Stoerzinger, A. Grimaud, J. Suntivich and Y. Shao-Horn, *Energy Environ. Sci.*, 2015, **8**, 1404–1427.
49 K. J. May, C. E. Carlton, K. A. Stoerzinger, M. Risch, J. Suntivich, Y.-L. Lee, A. Grimaud and Y. Shao-Horn, *J. Phys. Chem. Lett.*, 2012, **3**, 3264–3270.
50 R. Jacobs, J. Hwang, Y. Shao-Horn and D. Morgan, *Chem. Mater.*, 2019, **31**, 785–797.
51 J. Suntivich, K. J. May, H. A. Gasteiger, J. B. Goodenough and Y. Shao-Horn, *Science*, 2011, **334**, 1383–1385.
52 J. Suntivich, W. T. Hong, Y.-L. Lee, J. M. Rondinelli, W. Yang, J. B. Goodenough, B. Dabrowski, J. W. Freeland and Y. Shao-Horn, *J. Phys. Chem. C*, 2014, **118**, 1856–1863.